

Influence of deposition potential on the electrochemical growth and photocatalysis performance of SnO₂ nanostructures

Khadija Daideche^{a,c}, Halla Lahmar^b, Djahida Lerari^c, Amor Azizi^{a,*}

^a Laboratory of Chemistry, Molecular Engineering and Nanostructures, Chemistry Department, Faculty of Science, Ferhat Abbas-Sétif University, Sétif 19000, Algeria

^b Unit of Research in Nanosciences and Nanotechnologies (URNN), Center for Development of Advanced Technologies (CDTA), Ferhat Abbas-Sétif University, Sétif 19000, Algeria

^c Center for Scientific and Technical Research in Physical and Chemical Analysis (CRAPC), BP 384, Zone Industrielle Bou-Ismaïl RP 42004 Tipaza, Algeria

ARTICLE INFO

Keywords:

SnO₂
Nanocomposite
Nanostructures
Potential
Photocatalyst
SnO

ABSTRACT

In this paper, the effect of the deposition potential on characteristics, phase compositions and photocatalysis performances of SnO₂ nanostructures obtained by electrodeposition method was studied. A cyclic voltammetry was utilized to investigate the electrochemical behaviour of SnO₂ deposits. X-ray diffraction (XRD) analysis confirms the formation of a polycrystalline phase of rutile SnO₂ structures and a deterioration of SnO₂ crystallinity accompanied with the formation of SnO and Sn phases at a deposition potential of -1.3 and -1.5 V vs. SCE. Mott-Schottky plots confirm *n*-type conductivity of SnO₂ semiconductor and show high donor densities in the order of 10^{20} cm⁻³. The electrochemical impedance spectroscopy (EIS) measurements indicated a high separation of the photogenerated carriers for SnO₂-SnO nanocomposite deposited at -1.3 V. From field emission scanning electron microscopy (FE-SEM) images, a porous and homogenous SnO₂ deposit with ultra-fine nanoparticles were observed. Optical transmittance spectra and Tauc plots display a variation of transmittance and gap energy with the deposition potential variation. The highest transmittance of 44 % with largest gap energy of 4.17 eV were obtained for SnO₂ nanostructures deposited at -1.1 V. Photodegradation of MB organic dye using SnO₂ catalyst was confirmed for all samples and reached a maximum efficiency of 49 % for the SnO₂-SnO nanocomposite deposited at -1.3 V.

1. Introduction

The metal oxide semiconductor nanostructures are an important material which has been used extensively in many interesting applications. The beneficial characteristics of these materials, at the nanometer scale, such as high conductivity, transparency and large specific surface area facilitates their application in optoelectronic devices, gas sensors, batteries and photo catalysts [1–6]. Materials based on tin dioxide (SnO₂) nanostructures, such as nanocomposites heterostructures and elements doped SnO₂ have attracted a great research interest due to their excellent properties. The SnO₂ is a *n*-type semiconductor with a wide direct band gap ($E_g = 3.6$ eV at 300 K), a high chemical stability, high conductivity and transparency, good electrochemical performance and environment-friendly [7–9].

A considerable amount of recent literature has been published on the exploitation of materials based on SnO₂ nanostructures in different applications. For example, SnO₂ nanofibres, SnO₂/NiO and Co₃Sn₂/SnO₂

nanocomposites were utilized as anode material for sodium and Lithium-ion batteries, which results in a high and improved cycling capacity [9–11]. The SnO₂ nanoparticles and nanocrystals were employed in the photocatalytic degradation of dye methyl blue (MB), rhodamine B (RhB) and ppb-level acetaldehyde; the two materials show a high photocatalytic performance [7,12]. As well, Toloman and al. reported the application of SnO₂-TiO₂ nanocomposite heterostructures in the degradation of organic pollutants present in aqueous solution [13]. Other investigators have examined the Ni-doped SnO₂ nanoparticles as a sensor for the ammonia at ambient temperature and the SnO₂-SnO nanocomposites as a promising gas sensor for NO₂ gas detection [14,15]. SnO₂ quantum dots doped multiphase TiO₂ nanorods display a high photocatalytic water splitting [16]. In addition, a SnO₂/SnO/Sn nanocomposite reveals a high potential to improve the performance of Li-ion batteries [17].

Although extensive research has been carried out on materials based on SnO₂ nanostructures, the application of SnO₂-SnO-Sn

* Corresponding author.

E-mail addresses: aziziamor@yahoo.fr, amorazizi@univ-setif.dz (A. Azizi).

<https://doi.org/10.1016/j.inoche.2022.110154>

Received 22 August 2022; Received in revised form 25 October 2022; Accepted 27 October 2022

Available online 1 November 2022

1387-7003/© 2022 Elsevier B.V. All rights reserved.

nanocomposites as a photocatalyst has not yet been reported. Furthermore, the studies reported on SnO₂ based nanocomposite as photocatalyst have employed SnO₂ powder suspension dissolved in the dye solution to evaluate the photocatalytic efficiency [12,13]. This method requires additional centrifuging and filtration of the dye solution after the photocatalysis. In contrast, the photocatalytic efficiency of thin films is evaluated by a simple immersion in organic dye.

The novelty of this work is the preparation of SnO₂-SnO and SnO₂-SnO-Sn nanocomposite thin films with high photodegradation efficiency by a simple electrodeposition method. In this paper, SnO₂ nanostructures and SnO₂-SnO-Sn nanocomposites were electrodeposited on ITO substrates by the variation of the deposition potential as a key electrochemical parameter. Which can influence the phase composition, the physical properties and the photocatalysis performance of the electrodeposited semiconductor? The electrochemical, structural and optical properties of the obtained samples were characterized by different techniques. The photocatalytic activity of SnO₂ and SnO₂-SnO-Sn nanocomposite thin films was studied through the degradation of methylene blue dye organic pollutant.

2. Experimental

The electrodeposition and the electrochemical measurements (Chronoamperometry, Cyclic Voltammetry, Mott-Schottky and Electrochemical Impedance Spectroscopy) were carried out in a conventional three-electrode cell using a Volta-Lab 40 Potentiostat/Galvanostat controlled by a PC. The counter electrode and the reference electrode are a platinum wire electrode and a saturated calomel electrode (SCE, E°=0.241 vs HNE), all measurements were versus this reference.

For the electrodeposition of SnO₂ nanostructures, the working electrode was an indium tin oxide coated glass substrate (ITO: sheet resistance of 30 Ω/cm²) of 1 cm² exposure surface area. The pretreatment of the ITO substrates was as described in our previous report [18]. The electrodeposition was carried out under potentiostatic mode using chronoamperometry technique for 10 min deposition time. The electrolyte aqueous solution was consisting of 0.04 M SnCl₂ as precursor, 0.1 M NaNO₃ as supporting electrolyte and 0.1 M HNO₃ to maintain an acidic pH. The deposition temperature was fixed at 70 °C using a thermostatic bath. While, three different depositions potential values were applied: -1.1, -1.3 and -1.5 V. After the electrodeposition, the obtained samples were rinsed with distilled water and were dried in air under ambient conditions.

Cyclic Voltammetry (CV) and the Mott-Schottky (M-S) analysis were realized at room temperature and the working electrode was the SnO₂ nanostructures deposited at three different applied potentials. For CV study, the substrate was immersed in 0.1 M KCl solution under a scanning potential from 0 to -1.0 V with a scanning rate of 50 mVs⁻¹. From M-S analysis, the conduction type and the donor density were identified in 2 M NaNO₃ electrolyte under a frequency of 500 Hz. The electrochemical impedance spectroscopy (EIS) measurement was performed in aqueous electrolyte of 0.1 M NaNO₃ and frequency range from 50 Hz to 10 kHz.

The morphological characterization was obtained using field emission scanning electron microscopy (FE-SEM, Joel JSM-7001F). Phase identification and crystallographic structure of the samples were determined by X-ray diffraction (XRD) using the CuKα radiation (λ = 1.5406 Å) over an angular range of 20 to 80°. The optical properties were measured with a UV-Vis-NIR spectrophotometer (Shimadzu UV-1800) in the wavelength range of 200 to 100 nm.

The photocatalytic activity of SnO₂ nanostructures thin films was evaluated by degradation of 10⁻⁵ M methylene blue dye aqueous solution. All experiments were carried out in a dark room with destined opening to irradiate the samples by UV Lampe (254 nm and power of 12 W). The SnO₂ nanostructures layers elaborated at three different potential values -1.1, -1.3 and -1.5 V were immersed in 25 ml MB aqueous solutions to receive the UV irradiation for 3 h. After each

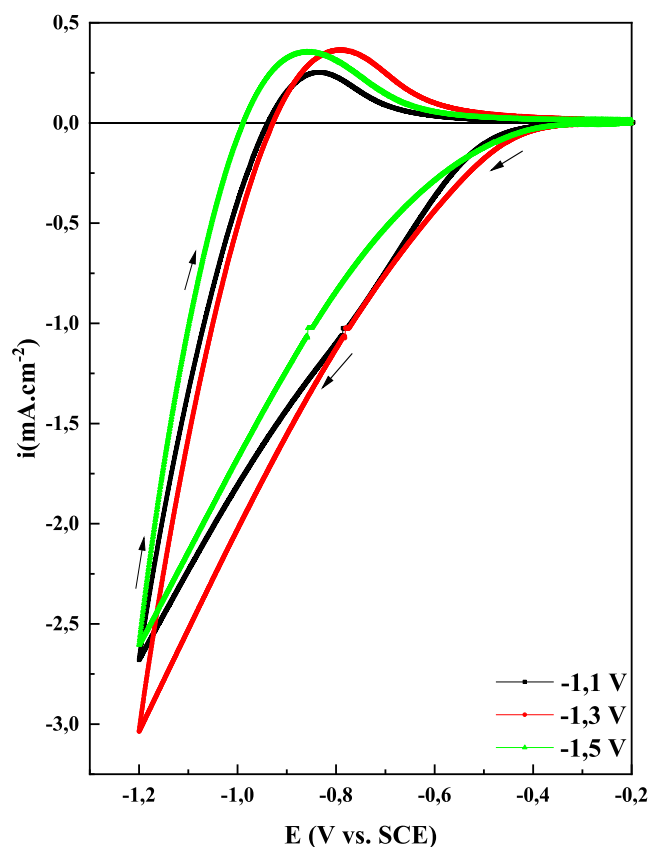


Fig. 1. Cyclic voltammograms of SnO₂ nanostructures obtained at three different deposition potentials in 0.1 M KCl with 50 mVs⁻¹ scan rate.

experiment, the decrease in absorption intensity of MB solution is studied using UV-Vis-NIR spectrophotometer (Shimadzu UV-1800).

3. Results and discussion

The cyclic voltammetry (CV) is a precise electrochemical method employed to investigate the reduction and oxidation process at the electrode-electrolyte interface. CV is a potentiodynamic technique that involves applying a potential sweep at a fixed scan rate and then recording a current density response resulting from redox reactions. To confirm the formation of SnO₂ nanostructures, the electrochemical behavior of the samples deposited at three different potentials was studied by cyclic voltammetry. The voltammograms of SnO₂ samples were carried out in 0.1 M KCl electrolyte with a scan rate of 50 mVs⁻¹ as illustrated in Fig. 1. As can be seen, all three samples show identical voltammogram shape. In the forward scan (cathodic scan), a cathodic current appeared at -0.45 V which indicates the reduction of SnO₂ to SnO and may be to the reduction of SnO to Sn, as shown in Eqs. (1) and (2) [19]. The marked increase of the cathodic current at about -1 V is associated with hydrogen evolution (Eq. (3)). In the back scan (anodic scan), the appearance of anodic peak related to the reversible oxidation of SnO to SnO₂ and may be correspond to the oxidation of Sn to SnO as ascribed in Eqs. (4) and (5), respectively. The current density of the anodic peak (i_{ap}) was 0.24, 0.35 and 0.34 mA/cm² for the samples deposited at -1.1, -1.3 and -1.5 V vs SCE, respectively. It is clear that the current density augmented by increasing the deposition potential from -1.1 to -1.5 V. Which can be explained by the increase of SnO amount in the samples deposited at -1.3 and -1.5 V, respectively; in comparison to that deposited at -1.1 V. This finding is confirmed by XRD analysis (Fig. 4), where the intensity of SnO diffraction peaks increased for the nanocomposites deposited at -1.3 and -1.5 V. It is important to note that the reversibility of SnO₂/SnO and the SnO/Sn

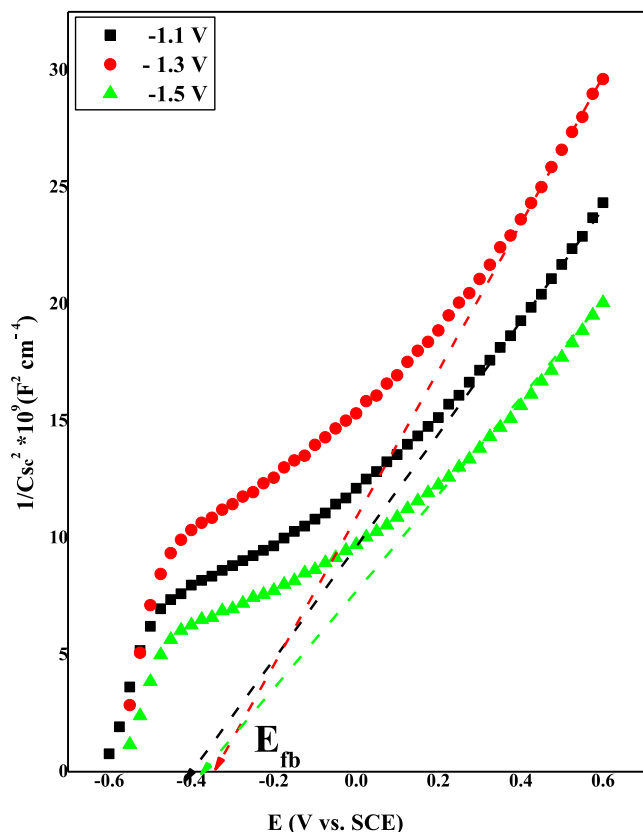
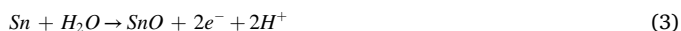


Fig. 2. Mott-Schottky plots of SnO₂ nanostructures obtained at three different deposition potentials in electrolyte 2 M NaNO₃.

redox couples is an advantage that promotes the application of SnO₂ and SnO₂-SnO-Sn nanocomposites as anode material in batteries.



In case of semiconductor (SC)/electrolyte contact, charges are exchanged between the SC and the redox couple in the electrolyte until equilibrium state, where the Fermi levels of the two materials are equal. In *n*-type SC, the electrons transfer from the SC to the redox couple presents in the electrolyte, charge carriers (electrons) are depleted in a zone named space charge layer (SCL) which becomes positively charged and the carrier densities are much lower than those of the electrolyte solution. The SCL is counterbalanced essentially by a layer of negative charge in electrolyte named Helmholtz layer, assimilates a parallel-flat capacitor. Assuming that the capacity of the Helmholtz layer is larger than that of the space charge region, the capacity of semiconductor passive layer follows the Mott-Schottky equation [20,21]:

$$\frac{1}{C_{SC}^2} = \frac{2}{\epsilon\epsilon_0qA^2N_D} \left[V - V_{fb} - \frac{KT}{e} \right] \quad (6)$$

where C_{SC}^2 is the semiconductor capacity, ϵ_0 is the vacuum permittivity, ϵ is the relative permittivity of the semiconductor, e the elementary charge, N_D the donor carrier concentration, V the applied potential, V_{fb} the flat band potential, T the thermodynamic temperature and K is the Boltzmann's constant. The study of the variation of the semiconductor

Table 1

The crystallographic parameters determined with respect to the peak (110) of SnO₂ nanostructures as a function of the deposition potential.

E (V vs. SCE)	-1.1	-1.3	-1.5	Standard Parameters
2θ (°)	26.49	26.65	26.45	26.59
β (°)	2.449	2.347	4.032	/
a (Å)	4.754	4.726	4.761	4.736
c (Å)	3.177	3.215	3.168	3.201
d ₁₁₀ (Å)	3.362	3.342	3.367	3.347
D (nm)	6.53	6.81	3.96	/
σ 10 ¹⁸ (lines/m ²)	5.48	5.09	14.79	/
ε (%)	0.59	0.57	0.98	/

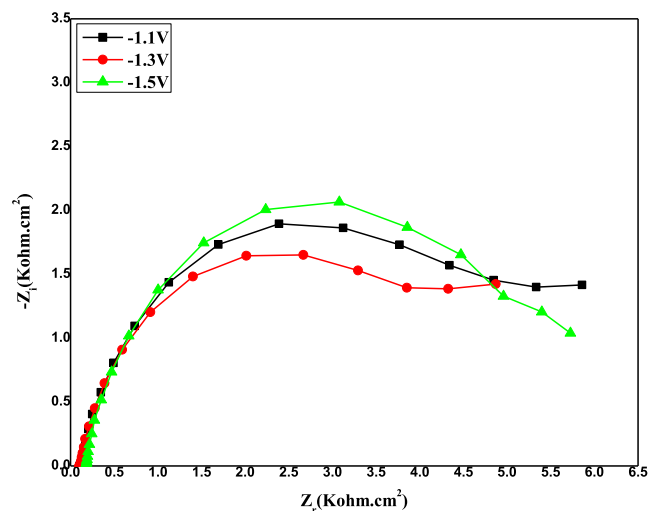


Fig. 3. Nyquist plots of SnO₂ nanostructures obtained at three different deposition potentials in electrolyte of 0.1 M NaNO₃.

capacitance in the space charge region ($1/C_{sc}^2$) as a function of the applied potential allows the identification of the semiconductor type and the estimation of the charge carrier density (N_D).

The Mott-Schottky plots of the samples obtained at three different deposition potentials were carried out in aqueous electrolyte of 2 M NaNO₃ with 500 Hz frequency as presented in Fig. 2. The plots present a straight-line part with positive slope which is in good agreement with Mott-Schottky equation of a *n*-type semiconductor [22,23]. The donor density is proportional to the inverse of the slope ($N_D = \frac{2}{\epsilon\epsilon_0qA^2} \times \frac{1}{slope}$,

$slope = \frac{d(\frac{1}{C_{sc}^2})}{dV}$) and the flat-band can be obtained by extrapolating the intercept with x-axis at $\frac{1}{C_{sc}^2} = 0$.

All the samples have a carrier concentration more than 10^{20} cm^{-3} , which is a positive factor for *n*-type semiconductor applications. When the deposition potential increase from -1.1 to -1.3 V, the carrier concentration decreases from 10.23×10^{20} to $4.93 \times 10^{20} \text{ cm}^{-3}$, respectively. A re-increase to a value of $6.95 \times 10^{20} \text{ cm}^{-3}$ was observed for -1.5 V. This dependence of the carrier concentration with the deposition potential may be due to the different phase composition in each sample as revealed in XRD patterns (Fig. 4). Where the sample composed of pure SnO₂ (deposited at -1.1 V) shows the highest N_D . On the other hand, the samples contain SnO and Sn impurity phases deposited at -1.3 and -1.5 V present lower carrier concentration due to the presence of SnO phase, which acts as p-type autoping in these nanostructures [24-26]. The re-increase of donor density for the samples obtained at -1.5 V could be attributed to the decrease in the crystallite size (Table 1).

The flat band potential (E_{fb}) values are -0.47, -0.32 and -0.37 V vs. SCE for the samples deposited at -1.1, -1.3 and -1.5 V, respectively.

The interface transfer/recombination rate of photogenerated carriers

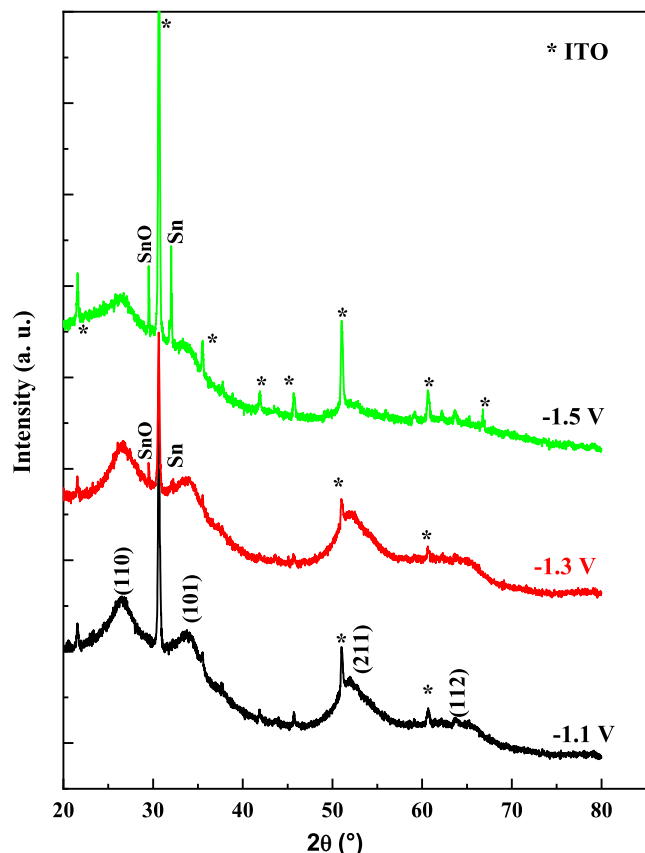


Fig. 4. XRD patterns of the SnO₂ nanostructures electrodeposited on ITO substrates at three different deposition potentials.

is an important factor that defines the photoactivity performance of a semiconductor. Therefore, the electrochemical impedance spectroscopy (EIS) measurement was performed to have a deep insight on the transfer/recombination process at the interface of SnO₂ samples. Fig. 3 displays the impedance spectra of the samples obtained at three different deposition potentials. The EIS diagrams were recorded in aqueous electrolyte of 0.1 M NaNO₃ and frequency range from 10 kHz to 50 Hz. As can be seen, the semicircle radius in the Nyquist plot changes by the variation of the deposition potential. The smallest radius was obtained for the sample deposited at -1.3 V. This indicates that the SnO₂-SnO nanocomposites have the most effective separation and the highest transfer of the photogenerated carriers compared to the other samples. This might be related to the formation of p-SnO/n-SnO₂ junction that facilitates the charge separation at the junction interface [27].

The phase purity and crystalline structure of the samples were studied using XRD measurements. The XRD patterns obtained from the deposits grown at three different potentials are presented in Fig. 4. The diffracting peaks correspond to ITO substrate are indicated by stars in the XRD patterns. All the samples present a polycrystalline tin oxide with tetragonal rutile structure (JCPDS card no. 88-0287). In particular, the nanostructures deposited at -1.1 V has a noticeable (110), (101), (211) and (112) orientations, signed to SnO₂ phase [28,29]. The broad and small diffraction peaks reflect the nanometric scale of the SnO₂ particles [6,30]. As shown in Fig. 4, the structure of the samples was sensitive to the deposition potential of SnO₂. The crystallinity of SnO₂ was changed by increasing the deposition potential and other diffraction peaks also appeared. We observed a decrease in the number and the intensity of the diffraction peaks correspond to SnO₂ phase for the sample deposited at higher potential -1.3 and -1.5 V, respectively. Especially the sample obtained at -1.5 V that revealed only one peak of SnO₂ (110). This designates the deterioration of SnO₂ phase

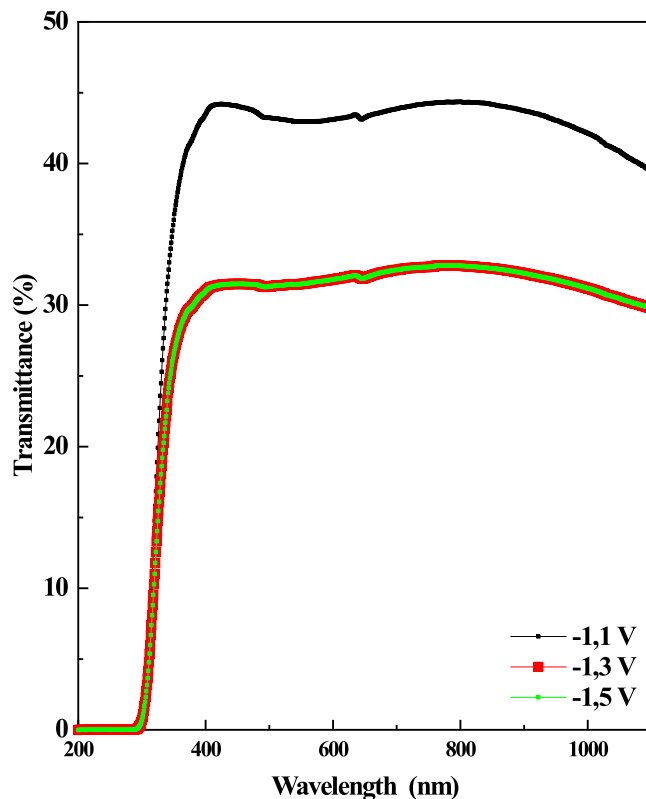


Fig. 5. FE-SEM images of SnO₂ nanostructures electrodeposited at three different deposition potentials: a) -1.1 V, b) -1.3 V and c) -1.5 V. a')-c') showing the higher magnification images of the same samples (40000x enlargements).

crystallinity with increasing the deposition potential [31]. Also, the presence of new peaks in the samples deposited at -1.3 and -1.5 V indicates the formation of secondary phases of tetragonal tin monoxide (SnO) at $2\theta = 29.74^\circ$ (JCPDS card no. 78-1913) and tetragonal metallic Sn at $2\theta = 32^\circ$ (JCPDS card no. 89-2958). This confirms the formation of SnO₂-SnO-Sn nanocomposites in the samples deposited at -1.3 and -1.5 V, while no peaks of other impurities were detected [34,35]. The reaction mechanisms proposed for the formation of SnO is similar to that of SnO₂ deposition detailed in our previous work and in several studies [18,33]. The reaction paths are ascribed as follow:



The presence of metallic Sn in these nanostructures can be explained by the close potential values of the reduction of nitrate ions to the reduction of Sn⁴⁺ to metallic Sn [18,34].

The crystallite size was estimated from the full-width at half-maximum (FWHM) of the (110) peak using the Scherrer's equation [35]:

$$D = \frac{0.9\lambda}{\beta \cos\theta} \quad (10)$$

where λ , β and θ are the X-ray wavelength of Cu K α_1 radiation ($\lambda = 1.54056 \text{ \AA}$), the full width at half maximum (FWHM) and the diffraction angle, respectively.

The values of the average crystallite size (D) are very small (Table 1) and are in agreement with the results of previous study [36]. It is clear that the deposition potential has a significant influence on all

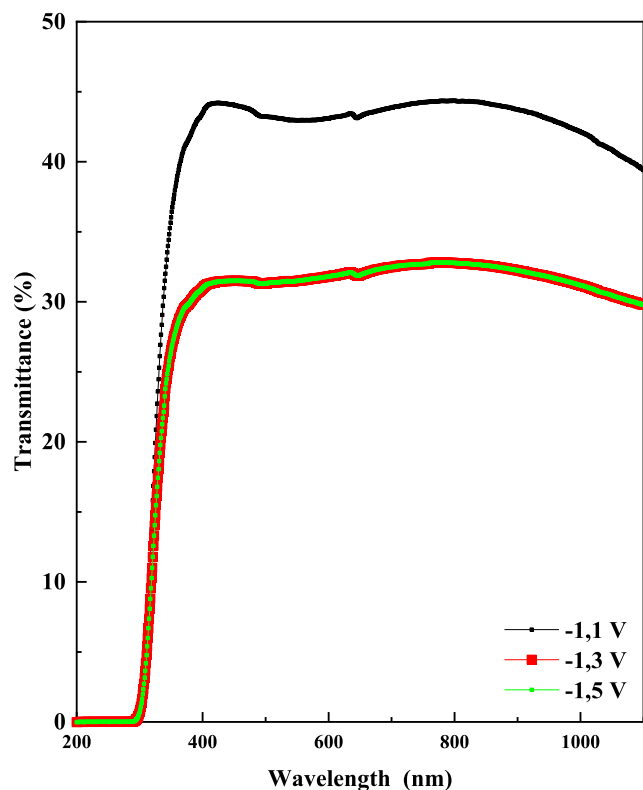


Fig. 6. Transmittance spectra of SnO₂ nanostructures electrodeposited on ITO substrate at three different deposition potentials.

crystallographic parameters (Table 1). Effectively, the observed d-spacing values of the (110) peak of SnO₂ nanostructures grown at three different applied potentials were compared with the reported values in JCPDS reference. The values of the calculated crystallographic parameters are very close to the standard values of tin oxide, with some differences in the sample deposited at -1.5 V that may be due by the constraints related to the existence of Sn impurities.

Based on the micro structural parameters, the defects density (σ) and microstrain (ϵ) can be calculated through the following relations [37,38]:

$$\sigma = \frac{1}{D^2} \quad (11)$$

$$\epsilon = \frac{\beta \cos \theta}{4} \quad (12)$$

where D is the average crystallites size and β the FWHM for the (110) peak. The defects density and microstrain of SnO₂ deposited at three different potentials are set out in Table 1. For the nanocomposites grown at -1.5 V, the high dislocation density value (14.79 lines/m²) is related to the decrease in the grain size.

Fig. 5 presents the field emission scanning electron microscopy (FE-SEM) images of the SnO₂ nanostructures at three different applied potentials. The FE-SEM images show a uniform, porous and homogenous deposit with ultra-fine nanoparticles. This can offer a large surface area with more reactive sites that improve the photocatalytic performances of these samples. The grain size decreases with increasing the deposition potential in addition to the formation of cracks on the surface of the samples deposited at -1.3 and -1.5 V, respectively. These cracks can be attributed to the acceleration of the concurrent reaction of hydrogen liberation in acidic medium. This inhibits the deposition of SnO₂ on the surface and eventually the appearance of cracks [39,40].

The optical transmission spectra of the samples obtained at three different applied potentials are shown in Fig. 6. The transmittance

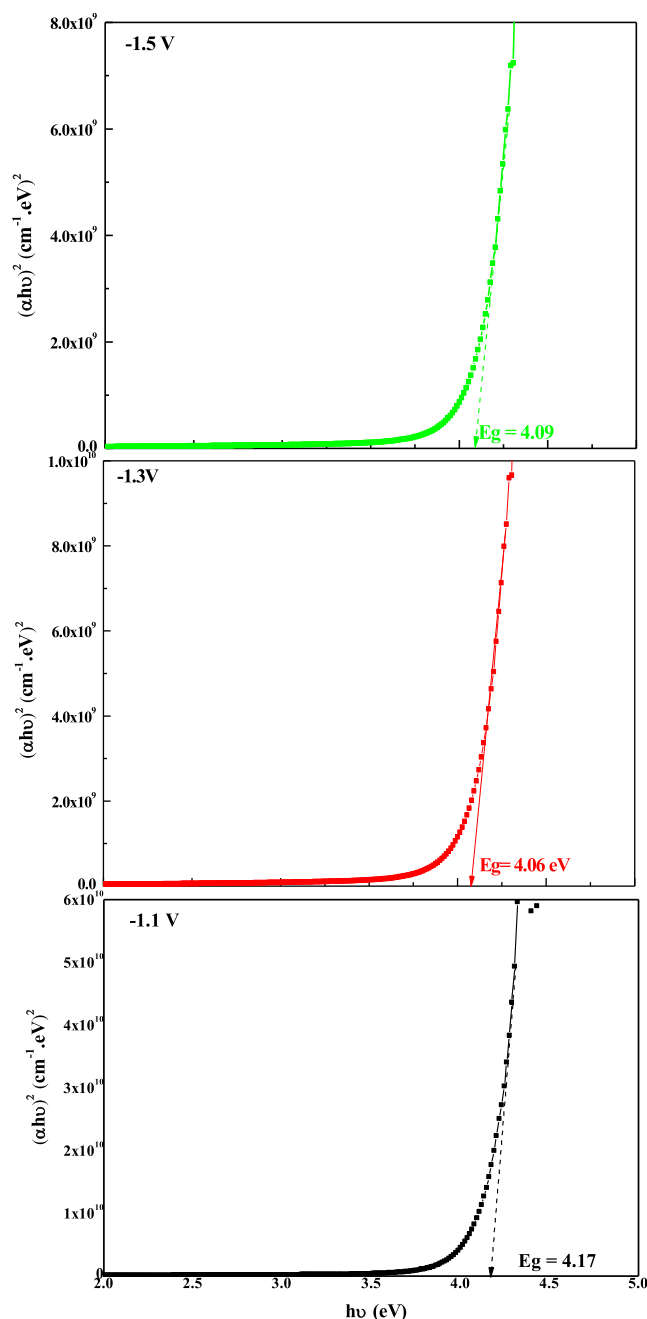


Fig. 7. Tauc plots of SnO₂ nanostructures electrodeposited on ITO at three different deposition potentials.

curves revealed an identical shape for all samples. The average values of transmittance in the visible range were 44 % for the sample deposited at -1.1 V and 32 % for the two other samples obtained at -1.3 and -1.5 V, respectively. It is important to note that the highest transmittance is obtained for -1.1 V which corresponds to the SnO₂ pure phase. This may be explained by the thickness increase with increasing the deposition potential demonstrates by chronoamperometry study (not shown here), which reduce the transmittance of the samples deposited at high potential. It is well established that the increasing of film thickness causes a high surface roughness which degrade the optical transparency; this effect is due to the increase of light scattering resulting from rough surface [41].

In order to estimate the optical gap energy (E_g) of SnO₂ nanostructures deposited at three different potentials, we plotted the Tauc characteristic curves using the following relation [42]:

$$(\alpha h\nu)^n = A(h\nu - E_g) \quad (13)$$

where h is the Planck's constant, ν is the photon frequency, α is the absorption coefficient, E_g is the band gap energy and A is the slope of the linear part of Tauc plot. The value of the exponent (n) denotes the nature of the electronic transition, whether direct or indirect, allowed or forbidden. For direct allowed transitions $n = 1/2$, for direct forbidden transitions $n = 3/2$, for indirect allowed transitions $n = 2$ and for indirect forbidden transitions $n = 3$. Fig. 7 illustrates the variation of $(\alpha h\nu)^2$ as a function of $h\nu$, the straight-line portion of the plots indicates the direct allowed transition in the tin oxide semiconductor [43]. The optical band gap energy (E_g) is determined by the interception of the linear part of the curve $(\alpha h\nu)^2$ with the energy axis at $(\alpha h\nu)^2 = 0$. The obtained E_g values were 4.17, 4.06 and 4.09 eV for the samples deposited at -1.1 , -1.3 and -1.5 V, respectively. The variation of E_g as a function of the deposition potential is related to the change in the phase composition, crystallinity, grain size and charge carrier density in each sample [41]. As can be seen from Fig. 7, the E_g decrease from 4.17 to 4.06 eV with increasing the deposition potential from -1.1 to -1.3 V, which is likely to be related to the decrease of donor density from 10.23×10^{20} to $4.95 \times 10^{20} \text{ cm}^{-3}$ for the sample deposited at -1.1 and -1.3 V, respectively. This effect is known as Moss-Burstein effect [44]. The re-increase of the gap energy to 4.09 eV for the sample formed at -1.5 V is related to the decrease of the crystallite size, shown in XRD result (Table 1). This is defined as the quantum size effect induced by the nanometric size of SnO_2 crystallites in these nanostructures [45,46].

The SnO_2 based nanocomposites are potential photocatalyst for the degradation of organic pollutants that was the subject of many studies. For example, the photocatalytic activity of SnO_2 and $\text{SnO}_2\text{-SnO}$ nanocomposites synthesized by electrochemical pulsed current in the MB degradation under UV irradiation was studied by Ulyankima et al. [47]. It was found that the degradation efficiency reaches 92.1 % during 30 min irradiation time. This high photocatalytic activity (in comparison to the individual SnO_2) was related to the inhibition of the photo-generated electron-hole recombination process by the efficient charge separation due to the formation of coupled semiconductor system $\text{SnO}_2\text{-SnO}$. Tammina et al. investigated the influence of SnO_2 nanoparticle size on the degradation of MB under UV irradiation [48]. 100 % degradation efficiency was reported and the smallest nanoparticles (3 nm) exhibited a higher degradation rate within a shorter time. The reason for this improvement was the large surface area of these nanoparticles that allows the adsorption of larger number of dye molecules on the particle surfaces. This enhances the interaction of adsorbed dye molecules with the free radicals generated on the nanoparticle surfaces. Another study by Dlugosz et al. [49] has examined the degradation of MB and RhB using $\text{ZnO-SnO}_2\text{-Sn}$ nanocomposites. The highest removal efficiency achieved was 96 % and 15 % under UV and visible light, respectively. The presence of SnO_2 was found to increase the photoactivity and extend the lifetime of the nanocomposite. While, the presence of Sn nanoparticles has ameliorated the activity under the visible light [49].

Since the utilization of catalyst in the form of powder suspension still exhibits a high photodegradation efficiency close to 100 %, all these recent studies utilized powder suspension of SnO_2 based nanocomposites as photocatalyst for dye degradation. However, the purpose of the present work is testing SnO_2 nanocomposites thin films fabricated by simple electrochemical deposition for MB photodegradation. In addition, we investigated the effect of the presence of Sn and Sn phases in the nanocomposite on the degradation efficiency. The photocatalysis experiment is carried out by a simple immersion of SnO_2 nanocomposites films in MB dye solution and then pulling them after the degradation without additional centrifuging and filtration of the dye solution to separate the catalyst powder.

The effect of the deposition potential on the methylene blue (MB) photocatalytic degradation by SnO_2 nanostructures was evaluated using UV-vis absorption spectroscopy. Since the samples obtained at -1.1 ,

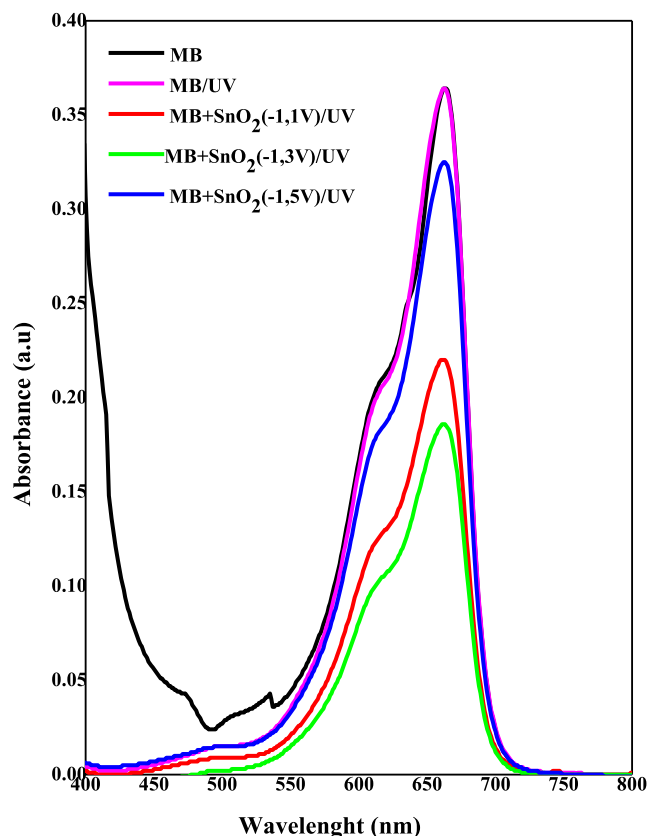


Fig. 8. Photodegradation plots of MB aqueous solution without and with the presence of SnO_2 catalyst nanostructures grown at three different deposition potentials.

Table 2

Photodegradation parameters of the MB organic dye by the SnO_2 catalyst nanostructures obtained at different deposition potentials..

	Absorbance	[MB] $\times 10^5$ mol/l	D (%)
MB	0.365	1.000	/
MB/UV	0.365	1.000	00
MB + SnO_2 (-1.1 V)/UV	0.222	0.608	39
MB + SnO_2 (-1.3 V)/UV	0.187	0.512	49
MB + SnO_2 (-1.5 V)/UV	0.325	0.890	11

-1.3 and -1.5 V applied potentials have a large band gap of 4.17, 4.06 and 4.09 eV, respectively; the photoactivation of the samples was carried out under a UV range sufficient energy ($\lambda = 254 \text{ nm}$). Fig. 8 shows the photo degradation plots of MB dye after 3 h continuous UV irradiation without and with the addition of SnO_2 catalyst nanostructures deposited at three different applied potentials. The dye degradation was monitored from the decrease of the intensity of MB dye absorption peak centred at 662 nm, along with the discoloration of the MB aqueous solution. As can be seen from Fig. 8, in the absence of SnO_2 photocatalyst and under a UV irradiation for 3 h the absorption intensity of MB was unchanged. This confirms that the direct photolysis is almost neglected. Another study reported efficiency less than 6 % of direct photolysis of MB dye under UV irradiation [43]. On the other hand, with adding SnO_2 catalyst deposited at three different potentials, a great decrease in the absorption intensity was noted. The degradation efficiency D (%) of the MB organic dye by the SnO_2 catalyst was calculated using the following formula [51]:

$$D(\%) = \frac{C_0 - C_t}{C_0} \times 100 \quad (14)$$

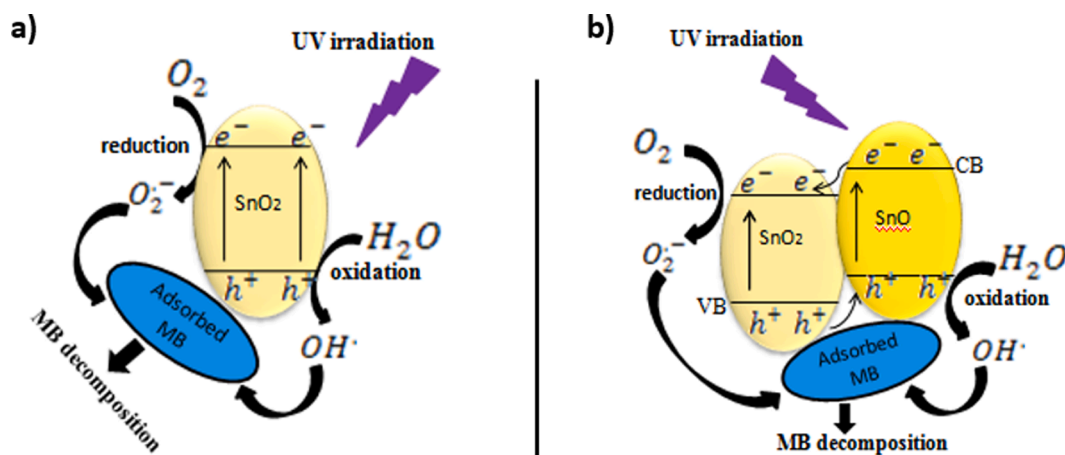


Fig. 9. Degradation mechanism for the MB dye by a) SnO_2 nanostructures and b) SnO_2 - SnO nanocomposite photocatalyst.

where and the dye concentration before and after the photodegradation, respectively. The obtained results are summarized in Table 2. The nanostructures grown at -1.1 and -1.3 V show degradation efficiency of 39 % and 49 %, respectively (Table 2). The amelioration of the photocatalytic efficiency of SnO - SnO_2 nanocomposite obtained at -1.3 V compared to that of the pure SnO_2 formed at -1.1 V can be due to the formation of p- SnO /n- SnO_2 heterojunction. The internal field built up in this junction facilitates an efficient migration of charge carriers leading to the high photocatalytic performance of SnO_2 - SnO nanocomposite [52]. This result is in agreement with EIS impedance (Fig. 3), that confirms an effective transport and separation of the photoinduced electron and hole in the sample deposited at -1.3 V due to the formation of p- SnO /n- SnO_2 heterojunction. On the other hand, the back down of the degradation efficiency for the samples obtained at -1.5 V may be explained by the increase of the amount of metallic Sn impurities as mentioned in XRD analysis (Fig. 4). Compared with other studies reported on the degradation of organic dye using SnO_2 thin films, the degradation efficiency of SnO_2 samples deposited at -1.1 V observed in this investigation (39 %) is far above those reported by Ayadi et al. [50]. In this study, Ce-doped SnO_2 thin film fabricated by spray pyrolysis shows an efficiency of 19 % for the degradation of MB dye under UV irradiation for 100 min. Also, close results to our finding were obtained by Roy et al. [53] which studied the MB degradation using SnO_2 powder suspension. A degradation efficiency of 34 % within 3 h irradiation under 400 W mercury vapor lamp was reported for pristine SnO_2 . Whereas, 64 % efficiency was obtained for SnO_2 - SnO nanocomposites [53].

The photodegradation mechanism of the different deposited samples can be explained as follows. For the pure SnO_2 deposited at -1.1 V (Fig. 9a), the illumination of SnO_2 film surface by enough UV light induced the formation of an electron (e^-) in the conduction band and a hole (h^+) in the valence band. The generated electron reduces the oxygen (O_2) adsorbed on the catalyst surface to oxygen radical (O_2^-). While, the hole oxidizes a water molecule to produce OH radicals (OH^*) that oxidizes the MB molecule [54]. The obtained OH^* and O_2^- radicals are a powerful oxidating species that degrade efficiently the MB dye molecules to CO_2 and H_2O [55]. On the other hand, the photodegradation of MB dye followed another process due to the formation of p- SnO /n- SnO_2 heterojunction in the nanocomposite deposited at a higher deposition potential (-1.3 V). Which results in a better degradation efficiency for this sample as explained above. As shown in Fig. 9b, the electron-hole pairs (e^- , h^+) are generated in SnO_2 and SnO then migrate to the junction interface that the separation of electron hole pairs. As a result of this, the electrons present in the conduction band of SnO_2 reduce the molecular oxygen to reactive superoxide radicals (O_2^-). Whereas, the holes present in the valence band of SnO produces hydroperoxyl radicals

(OH^*) by the oxidation of H_2O molecules. Then OH^* and O_2^- radicals oxidize the MB dye. For the SnO_2 - SnO - Sn nanocomposite deposited at -1.5 V, the high amount of Sn present in this sample reduced the MB photodegradation efficiency.

4. Conclusion

In summary, the deposition potential had a great effect on the different properties of the tin oxide nanostructures obtained by electrodeposition on ITO substrate. Cyclic voltammetry shows redox reversibility of the SnO_2 / SnO couple. A n -type conductivity and a variation of the charge carrier concentration with the deposition potential were observed. A high separation of the photogenerated carriers was confirmed for SnO_2 - SnO nanocomposite deposited at -1.3 V. An ultrafine and uniform morphology of SnO_2 nanostructures is noted with a decrease in grain size with increasing the deposition potential. XRD analysis shows the formation of SnO_2 polycrystalline structure at -1.1 V and a degradation of the crystallinity of SnO_2 with the formation of SnO_2 - SnO - Sn nanocomposite by increasing the deposition potential to -1.3 and -1.5 V. The optical properties are influenced by the deposition potential where the highest transmittance of 44 % is obtained at -1.1 V with large optical gap energy of 4.17 eV. A high photodegradation efficiency of 49 % is attributed to the nanocomposite deposited at -1.3 V, which suggests the application of SnO_2 - SnO nanocomposites as photocatalyst for degradation of organic pollutants.

Declaration of Competing Interest

The authors declare that they have no known competing financial interests or personal relationships that could have appeared to influence the work reported in this paper.

Data availability

No data was used for the research described in the article.

Acknowledgments

This work was funded under the Algerian General Directorate of Scientific Research and Technological Development (DGRSDT)/MESRS.

References

- [1] A. Allag, R. Saad, A. Ouahab, H. Attouche, N. Kouidri, *Chin. Phys. B* 25 (4) (2016) 04680.
- [2] Y. F. Sun, S. B. Liu, F.L. Meng, J.Y. Liu, Z. Jin, L.T. K. and J. H. Liu, *Sensors*, 12 (2012) 2610–2631.
- [3] M. Guncheva, M. Dimitrov, D. Zhiryakova, *Catal. Commun.* 16 (2011) 205–209.

- [4] Jun Song Che, and Xiong Wen (David) Lou, *Materials Today*, **15** (2012) 246–254.
- [5] W. Yan, F.A.N. Cai-me, H.B.L. Zhen-hai, S.U.N. Yan-pin, *Trans. Nonferrous Met. Soc. China* **19** (2009) 778–783.
- [6] J. Long, W. Xue, X. Xie, G.u. Quan, Y. Zhou, Y. Chi, W. Chen, Z. Ding, X. Wang, *Catal. Commun.* **16** (2011) 215–219.
- [7] D. Chu, J. Mo, Q. Peng, Y. Zhang, Y. Wei, Z. Zhuang, Y. Li, *Chem. Cat. Chem.* **3** (2011) 371–377.
- [8] A. Kar, A. Patra, *Trans. Ind. Ceram. Soc.* **72** (2) (2013) 89–99.
- [9] D. Zhang, C. Bi, Q. Wu, G. Hou, G. Zheng, M. Wen, Y. Tang, *New J. Chem.* **43** (2019) 1238.
- [10] E.C. Duran, H. Kizil, *ECS Trans.* **77** (11) (2017) 353–363.
- [11] C. Kim, J.W. Jung, K.R. Yoon, D.Y. Youn, S. Park, I.D. Kim, *ACS Nano* **10** (12) (2016) 11317–11326.
- [12] Y. Li, Q. Yang, Z. Wang, G. Wang, B. Zhang, Q. Zhang, D. Yang, *J. Name.* **00** (2013) 1–9.
- [13] D. Toloman, O. Pana1, M. Stefan, A. Popa, C. Leostean, S. Macavei, D. Silipas, I. Perhaita, M. D. Lazar, L. B. Tudoran, *J. Colloid Interface Sci.*, **542** (2019) 296–307.
- [14] M. Kandasamy, A. Seetharaman, D. Sivasubramanian, A. Nithya, K. Jothivenkatachalam, N. Maheswari, M. Gopalan, S. Dillibabu, A. Eftekhari, A.C. S. Appl. Nano Mater. **1** (10) (2018) 5823–5836.
- [15] L. Li, C. Zhang, W. Chen, *Nanoscale* **7** (2015) 12133–12142.
- [16] B. Sun, Y. Chen, L. Tao, H. Zhao, G. Zhou, Y. Xia, H. Wang, Y. Zhao, A.C.S. Appl. Mater. Interfaces **11** (2) (2019) 2071–2081.
- [17] J. Zhang, Z. Ma, W. Jiang, Y. Zou, Y. Wang, C. Lu, *J. Electroanal. Chem.* **767** (2016) 49–55.
- [18] K. Daideche, A. Azizi, *J. Mater. Sci.: Mater. Electron.* **28** (2017) 8051–8060.
- [19] R. Ma, Y.L. Chen, Y. Shen, H. Wang, W. Zhang, S.S. Pang, J. Huang, Y. Han, Y. Zhao, *RSC. Adv.* **10** (2020) 22828–22835.
- [20] K. Gelderman, L. Lee, and S. W. Donne, *J. Chem. Edu.*, Vol. **84** No. 4 April 2007.
- [21] K. Darowicki, S. Krakowiak, P. Slepki, *Electrochimica Acta* **51** (2006) 2204–2208.
- [22] F. Cardon, W.P. Gomet, *J. Phys. D.* **11** (1978) L63–L67.
- [23] R. Xie, J. Su, M. Li, L. Guo, *Int. J. Photoenergy* **7** (2013) ID 620134.
- [24] Y. Wang, N. Herro, *J. Phys. Chem.* **95** (1991) 525.
- [25] C.W. Ou, Z.Y. Dhananjay, Y.C. Ho, S.S. Chuang, M.C.W. Cheng, K.C. Ho, C.W. Chu, *Appl. Phys. Lett.* **92** (2008), 122113.
- [26] H.R. Kim, G.H. Lee, D.H. Kim, *J. Phys. D: Appl. Phys.* **44** (2011), 185203.
- [27] S. Li, J. Pan, H. Li, Y. Liu, W. Ou, J. Wang, C. Song, W. Zhao, Y. Zheng, C. Li, *Chem. Eng. J.* **366** (2019) 305–312.
- [28] S. Thiagarajan, T.H. Tsai, S.M. Chen, *Int. J. Electrochem. Sci.* **6** (2011) 2235.
- [29] D. Lee, D.Y. Yun, Y.S. No, J.H. Hwang, C.H. Lee, T.W. Kim, *J. Nanosci. Nanotechnol.* **13** (2013) 7596.
- [30] M. Guan, X. Zhao, L. Duan, M. Cao, W. Guo, J. Liu, W. Zhang, *J. Appl. Phys.* **114** (2013), 114302.
- [31] S. Kim, H. Lee, C.M. Park, Y. Jung, *J. Nanosci. Nanotechnol.* **12** (2012) 1616.
- [32] Z. Chen, Y. Tian, S. Li, H. Zheng, W. Zhang, *J. Alloys Compd.* **515** (2012) 57–62.
- [33] S.T. Chang, I.C. Leu, M.H. Hon, *J. Alloys Compd.* **403** (2005) 335–340.
- [34] L. Anicai, A. Petica b, S. Costovici, P. Prioteasa, T. Visan, *J. Electrochimica Acta*, **114** (2013) 868–87.
- [35] W Sutapa1, A.W. Wahab, P. Taba, N.L. Nafie, *J. Phys.: Conf. Ser.* **979** (2018) 012021.
- [36] A. Runa, H. Bala, Y. Wang, J. Chen, B. Zhang, H. Li, W. Fu, *Appl. Phys. Lett.* **105** (2014), 053102.
- [37] A. Zarkov, A. Stanulis, L. Mikoliunaite, A.N. Salak, A. Kareiva, *Thin Solid Films* **649** (2018) 219–224.
- [38] G. Yang, Z. Haibo, Z. Biying, *J. Mater. Sci.* **35** (2000) 917.
- [39] H. Faid, L. Mentar, M.R. Khelladi, A. Azizi, *Surf. Engin.* **33** (2017) 529.
- [40] D. Chu, Y. Masuda, T. Ohji, K. Kato, *Chem. Eng. J.* **168** (2011) 955.
- [41] A.A. Yadav, *Thin Solid Films* **591** (2015) 18–24.
- [42] J.B. Coulter, D.P. Birnie, *Phys. Status. Solidi B* (2017) 1700393.
- [43] H. Kim, C.M. Gilmore, A. Pique, J.S. Horwitz, H. Mattoussi, *J. Appl. Phys.* **86** (1999) 6451–6461.
- [44] J. Enriquez, X. Mathew, *Sol. Energy Mater. Sol. Cell.* **76** (2003) 313.
- [45] A. Karpuz, H. Kockar, M. Alper, *Appl. Surf. Sci.* **358** (2015) 605.
- [46] F. Gu, S.F. Wang, M.K. Lü, G.J. Zhou, D. Xu, D.R. Yuan, *J. Phys. Chem. B* **108** (2004) 8119.
- [47] A.A. Ulyankina, A.B. Kuriganova, N.V. Smirnova, *Mendeleev Commun.* **29** (2019) 2015–2017.
- [48] S.K. Tammuna, B.K. Mandal, N.K. Kadiyala, *Environ. Nanotechnol. Monitor. Manage.* **10** (2018) 339–350.
- [49] O. Długosz, M. Banach, *Appl. Nanosci.* **11** (2021) 1707.
- [50] M. Ayadi, O. Benhaoua, M. Sebais, O. Halimi, B. Boudine, M.S. Aida, *Res. Mater. Res. Express* **6** (2019), 076407.
- [51] P. Singh, G. Kaur, K. Singh, B. Singh, M. Kaur, M. Kaur U. Krishnan, M. Kumar, R. Bala, A. Kumar, *Appl. Nanosci.*, **8** (2018) 1–9.
- [52] S. Joshi, S.J. Ippolito, S.V. Manorama, *RSC Adv.* **10** (2016) 1039.
- [53] A. Roy, S. Arbu, Y. Waghadkar, M. Shinde, G. Umarji, S. Rane, K. Patil, S. Gosavi, R. Chauhan, *J. Solid State Electrochem.* **21** (2017) 9–17.
- [54] G. Elango, S. Manoj Kumaran, S.S. Kumar, S. Muthuraja, S.M. Roopan, *Spectrochimica Acta Part A: Mol. Biomol. Spectrosc.* **145** (2015) 176–180.
- [55] A.M. Al-Hamdi, U. Rinner, M. Sillanpää, *Process Saf. Environ. Protect.* **107** (2017) 190.

Dr. Khadija Daideche, is currently advisor research engineer at the Center for Scientific and Technical Research in Physico-Chemical Analysis (CRAPC, Algeria) and associate researcher in the Laboratory of Chemistry, Molecular Engineering and Nanostructures, Ferhat Abbas- Sétif University-Algeria. Research interests have been mainly focused on electrochemical fabrication of nonmaterial's for electrochemical, environmental and energy applications.



Djahida Lerari is Research Director and head of the Materials Chemistry Division at the Center for Scientific and Technical Research in Physico-Chemical Analysis (CRAPC, Algeria) and associate researcher at the Macromolecular Synthesis Laboratory at University of Science and Technology (USTHB, Algeria). Dr. Lerari research interests have been mainly focused on composites and nanocomposites with improved physical properties.



Dr. Azizi Amor is currently a professor at the Department of Chemistry, Faculty of Science, and the founder of the Laboratoire de Chimie, Ingénieries Moléculaire et Nanostructures (LCIMN), Université Ferhat Abbas-Sétif-Algeria. He received his Ph.D. degree in Engineering Matériaux from Strasbourg University, France in 1996. His research interest includes electrochemical nucleation and growth, electrochemical nano-engineering of Transparent Conducting Oxide nanostructures for photovoltaic, photonic, Photoelectrochemistry applications, control of microstructure and properties of nanostructures using electrochemical deposition (miniaturization, Interconnection,...). He has published more than 80 high impact journals.